Catalytic Ammonia Synthesis by Supported Molybdenum Nitride: Insight into the Support Effect

Amanda Sfeir, Camila Abreu Teles, Herve Vezin, Maya Marinova, Jean-Philippe Dacquin, S. Laassiri, Sebastien Royer

ChemCatChem

Research Article
doi.org/10.1002/cctc.202400494

Chemistry Europe
European Chemical Societies Publishing

www.chemcatchem.org

Catalytic Ammonia Synthesis by Supported Molybdenum Nitride: Insight into the Support Effect

Amanda Sfeir,[a] Camila A. Teles,[a] Hervé Vezin,[b] Maya Marinova,[c] Jean-Philippe Dacquin,[a] Said Laassiri,*[d] and Sébastien Royer*[a, e]

The influence of the support on the performance of Mo nitrides has been investigated in ammonia synthesis and decomposition. A series of Mo–N catalysts supported on different materials, namely SiO_2 (commercial, SBA-15), Al_2O_3, and CeO_2, were prepared. The results indicated that, despite the high dispersion of Mo species in all catalysts, large disparities in the activity for ammonia synthesis exist. Initial rates of ~1208, ~481, and ~372 μmol $g_{active\ phase}^{-1}$ h^{-1} are obtained over 10-Mo–N/SBA-15, 10-Mo–N/SiO_2, and 10-Mo–N/Al_2O_3 respectively. However, no catalytic activity was registered when Mo species were supported on CeO_2. Furthermore, 10-Mo–N/Al_2O_3 deactivated after few hours of reaction. The surface composition was studied by means of XPS to probe the origin of the catalytic activity differences, and the results indicated that a range of various oxidation states of Mo was detected depending on the support. The difference in catalytic behavior could not be solely explained by the differences in Mo–N species concentrations. In situ EPR analysis exhibited that the mechanism of MoO_3 nitridation could differ depending on the support, leading to the formation of different Mo–N species. The effect of support was, however, not as severe in ammonia decomposition as it was the case of ammonia synthesis.

1. Introduction

Ammonia (NH_3) possesses unique physicochemical characteristics, which enables it to play a major role in mid- and long-term storage of hydrogen and transportation[1] NH_3 is also being considered for direct energy generation as fuel in combustion engines for commercial maritime and aviation[2] as well as a potential energy carrier for fuel cells.[3] Furthermore, NH_3 is an important nitrogen building block for almost all high-value nitrogen-containing products, including nitric acid, urea, nitrogen-based fertilizers, and so forth. The transformation of highly stable atmospheric N≡N into the reactive nitrogen building block NH_3 via the Haber–Bosch (H–B) process has been instrumental in the industrialization of nitrogen-based fertilizer production. This in turn sustains a large fraction of human population by ensuring the availability of nitrogen-based fertilizers for intensive agriculture.

Despite its potential in decarbonizing both the energy and agricultural sectors, ammonia production remains closely tied to hydrogen production from nonrenewable fossil-based feedstock. Currently, the industrial production of ammonia is dominated by the H–B process in which highly purified N_2 and H_2 react over a promoted iron-based catalyst under high pressure (up to 200 bar) and temperature varying between 400 and 500 °C. The decarbonization of the H–B process has driven much research effort, especially in replacing hydrogen derived from fossil fuels by green hydrogen generated by water electrolysis powered by renewable energy. However, the development of a decarbonized H–B process capable of coping with the intermittency and uneven geographic distribution of renewable energy still requires further optimization in several of the H–B components. A key component where innovation and optimization have the potential to reshape the H–B process is the development of novel catalytic materials that are active under milder synthesis conditions.

Over the last years, numerous materials with enhanced catalytic properties, compared to the industrial doubly promoted iron-based catalyst, have been reported in the literature. Among these materials, Ru on activated carbon has driven significant interest due to its high catalytic activity, leading to the

[a] A. Sfeir, C. A. Teles, J.-P. Dacquin, S. Royer
Université de Lille, CNRS, ENSCL, Centrale Lille, Univ. Artois, UMR 8181-UCCS-Unité de Catalyse et de Chimie du Solide, Lille F-59000, France
E-mail: sebastien.royer@eilco.univ-littoral.fr

[b] H. Vezin
Laboratoire de Spectroscopie pour Les Interactions La Réactivité et L'Environnement UMR CNRS 8516-LASIRE, Université de Lille, Lille 59000, France

[c] M. Marinova
Université de Lille, CNRS, INRA, Centrale Lille, Université Artois, FR 2638 – IMEC – Institut Michel-Eugène Chevreul, Lille 59000, France

[d] S. Laassiri
Chemical & Biochemical Sciences, Green Process Engineering (CBS), Mohammed VI Polytechnic University, UM6P, Benguerir 43150, Morocco
E-mail: said.laassiri@um6p.ma

[e] S. Royer
Université Littoral Côte d'Opale, UR 4492, UCEIV, Unité de Chimie Environnementale et Interactions sur le Vivant, SFR Condorcet FR CNRS 3417, Dunkerque F-59140, France

[Correction added on 19 November 2024, after first online publication: Sébastien Royer's email address was updated in this version.]

Supporting information for this article is available on the WWW under https://doi.org/10.1002/10.1002/cctc.202400494

development of the Kellogg advanced ammonia process (KAAP). In these catalysts, the B_5 site in Ru nanoparticles has been identified as the active site with the most suitable energetic properties for nitrogen activation and dissociation at low temperatures.[4] As ammonia synthesis is a structure-sensitive reaction over Ru based catalysts, the catalytic performance is impacted by the electronic and geometric properties of the active site. Therefore, considerable effort has been directed towards promoting the catalytic activity through (i) doping by alkali and alkaline earth promoters[5] and/or (ii) modifying the nature of the support.[6] Consequently, exceptionally high catalytic activity has been reported, with significant influence from the support, for Ru. Although Ru supported on advanced supports (electrides, hydrides, perovskites) leads to high catalytic activity, its high cost and scarcity remains barriers to its widespread utilization in the industry. Nevertheless, the remarkable effect of a support in tuning the catalytic activity of Ru showcases the importance of modulating the support-active site interaction in ammonia synthesis. Given the aforementioned considerations, the development of alternative materials with reasonable catalytic activity, low-cost, and readily availability is of paramount importance. Molybdenum-based materials display high catalytic activity in multiple reactions, including hydrodesulfurization (HDS),[7] oxidative desulfurization,[8] CO_2 conversion,[9] ammonia synthesis,[10] and decomposition.[11] The catalytic activity of the γ-Mo_2N phase, in ammonia synthesis, has been reported as early as 1986 by the work of Volpe and Boudart[10b] and Oyama.[10c] However, the strong interaction between Mo and nitrogen/NH_x intermediate species results in limited catalytic activity in ammonia synthesis. Over the years, several strategies has been adopted to increase the catalytic activity of Mo by (i) addition of second metal resulting in the formation of bimetallic molybdenum nitrides/carbides (Co_3Mo_3N, Co_3Mo_3C, and Ni_2Mo_3N),[10a,12] in turn displaying optimized nitrogen binding properties, and (ii) dispersion of Mo species on suitable supports (MoN_x/ZSM-5, Mo_2C/CeO_2, and Mo/SBA-15).[10b,13] These modifications alter the structural and electronic properties of Mo, leading to significantly different catalytic behaviors and promote different reaction mechanisms. In the literature, detailed studies on the effect of the nature of the support in tuning the physicochemical properties of Mo species and therefore their catalytic activity are scarce due to the challenges associated with the characterization of Mo–N NPs species formed during the nitridation process. Nevertheless, the nature of the interaction between Mo and support species might also negatively impact the catalytic activity and lead to its premature deactivation. For example, strong interaction between Mo–Ti has been reported to alter the nitridation mechanism of Mo species when compared to a nonreducible support, leading to a complete turnoff of the catalytic activity in ammonia synthesis.[13c]

In this work, the effect of support and Mo-support interaction has been studied using Mo supported on common catalyst supports, namely CeO_2, Al_2O_3, SiO_2, and SBA-15. The identity of the active phase formed during the nitridation process has been identified by advanced characterization techniques such as in situ EPR and XPS. The performances of supported Mo–N species in ammonia synthesis and ammonia decomposition were investigated to understand how the support impacts the catalytic activity of ammonia synthesis. The results provided valuable insights into the design and optimization of catalysts for various catalytic applications, particularly in ammonia synthesis.

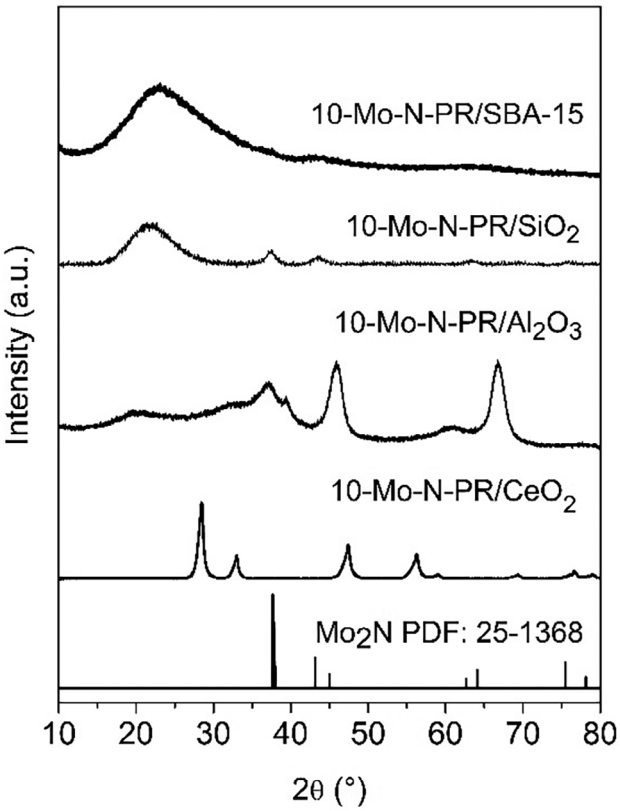

Figure 1. XRD diffractograms of the supported Mo–N catalysts after 20 h of reaction under ammonia synthesis conditions.

2. Results

2.1. Catalyst Characterization

Figure 1 displays the XRD of postreaction catalysts obtained after 20 h under ammonia synthesis conditions. The formation of Mo–N species, which are the known active species in ammonia synthesis, is usually obtained after the pretreatment step at 700 °C under 75 vol% H_2/N_2 (BOC, 99.98%) gas mixture at a total gas flow of 60 mL min^{-1} for 2 h.[14] This was verified by the nitridation of molybdenum oxide α-MoO_3 into β-Mo_2N (PDF 25-1368) under these conditions (Figure S1). However, upon nitridation and ammonia synthesis test, no diffraction peaks related to Mo–N species have been detected for 10-Mo–N-PR/Al_2O_3, 10-Mo–N-PR/CeO_2, and 10-Mo–N-PR/SBA-15, suggesting that the active phase do not crystallize or is well dispersed within these supports. On the other hand, in the case of 10-Mo–N-PR/SiO_2, poorly defined and broad peaks at $2\theta = 37.8°$, 43.4° and, 64.2° are assigned to the β-Mo_2N phase (PDF 25-1368), reflecting the formation of molybdenum nitride with limited crystallite size over this support. With the use of SBA-15 silica support, the β-Mo_2N peaks broadened to become barely visible in the signal baseline.

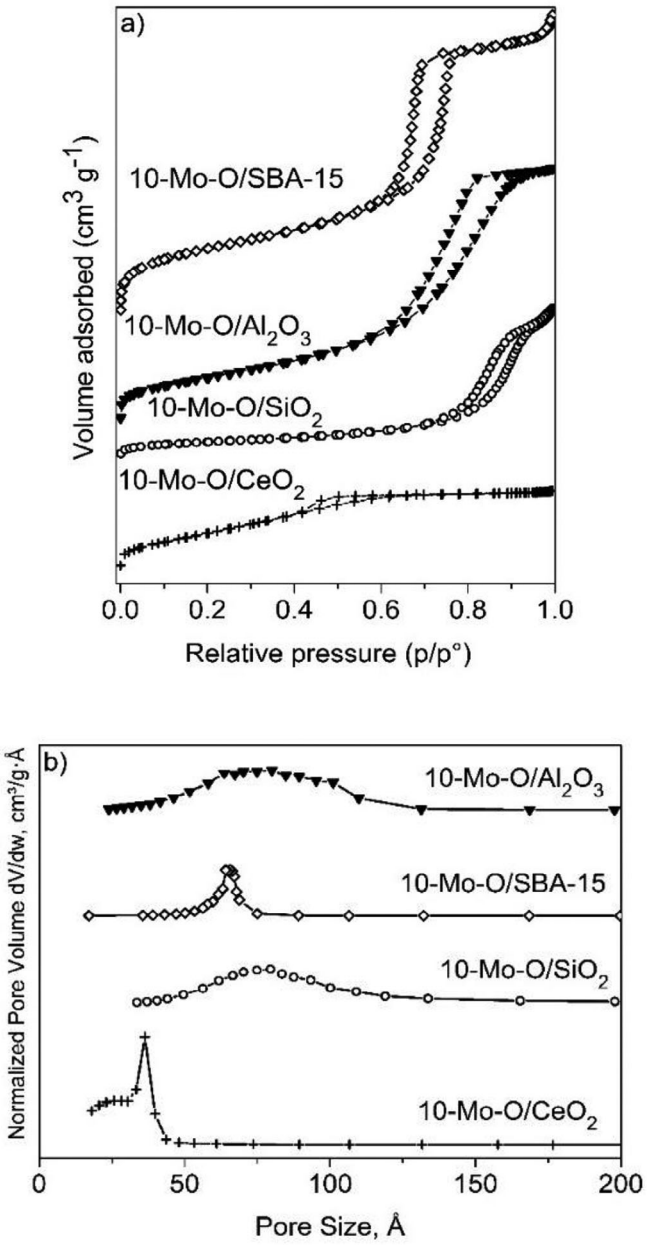

Figure 2. (a) N_2 adsorption–desorption isotherms and (b) BJH pore size distribution measured for the Mo–O supported materials.

2.1.1. Nitrogen Adsorption–Desorption Analysis

The nitrogen adsorption–desorption isotherms of the freshly calcined catalysts and their corresponding pore volume and pore size distribution are shown in Figure 2 and Table 1. In all the studied materials, a predominant type IV isotherm characteristic of mesoporous materials is observed. However, the characteristics of the hysteresis loop differ from one material to another, which reflects differences in the porosity and aggregate morphology of the solid supports. For instance, only CeO_2 and SBA-15 displayed a narrow pore size distribution centered at ~3.0 nm and 6.6 nm, respectively. However, the BET surface area and pore volume of CeO_2 were 194 $m^2\ g^{-1}$ and 0.16 $cm^3\ g^{-1}$, whereas SBA-15 displayed significantly higher surface area, ~465 $m^2\ g^{-1}$, and pore volume, 0.82 $cm^3\ g^{-1}$. In the case of 10-Mo–O/Al_2O_3 and 10-Mo–O/SiO_2 samples, much broader pore size distributions are observed with respect to CeO_2 and SBA-15. The surface area of 10-Mo–O/Al_2O_3 and 10-Mo–O/SiO_2 was 208 $m^2\ g^{-1}$ and 262 $m^2\ g^{-1}$, respectively. It is worth noting that upon Mo impregnation, only a small decrease in the surface area is observed with respect to the surface areas measured on the parent materials Al_2O_3, SiO_2 and CeO_2 (Table 1). Interestingly, the BET surface area of SBA-15 exhibited a more pronounced decrease after Mo loading (from 760 to 465 $m^2\ g^{-1}$).

The evolution of the surface area was also accompanied with a decrease in pore volume from 1.1 to 0.82 $cm^3\ g^{-1}$, resulting probably from partial clogging of the support porosity, associated with the impregnated phase confining in cylindrical channel-type porosity of SBA-15.[15]

2.1.2. HAADF–TEM Analysis

Upon activation, the morphology of supported Mo–N species as well as the element local distribution were studied by means of HAADF–TEM analysis coupled with EDS. Representative high resolution HAADF images for the 10-Mo–N/support catalysts are reported in Figure 3 and Figure S2.

In HAADF images, where the intensity is proportional to the atomic number of the element ($Z^{1.7}$), Mo atoms appear brighter on Al_2O_3, SBA-15, and SiO_2. In these materials, the mean particle size of Mo species has been estimated and the results are reported in Table 1. For siliceous-based supports, the mean particle size of Mo species was found to be ~2.9 ± 0.3 nm and ~1.3 ± 0.3 nm on SiO_2 and SBA-15, respectively (Figure 3). These differences are in line with XRD results, where broad XRD peaks characteristic of β-Mo_2N are detected when Mo-species are supported on SiO_2 but barely observed on SBA-15. In the 10-Mo–N/Al_2O_3 catalyst, the mean particle size was found to be ~1.7 ± 0.1 nm, which is in the same range of order as the particle size measured in the 10-Mo–N/SBA-15 sample. Unfortunately, in the case of 10-Mo–N/CeO_2, as the atomic number Z of Mo is lower as compared to Ce, Mo species could not be detected in the HAADF images (Figure 3c), and the d spacing visible in Figure 3c is associated to CeO_2 crystallographic structure. Complementary EDS analysis, presented in Figure S2, confirmed the high dispersion of Mo species in all the different supports. Unfortunately, due to limitations related to Mo small particle size, low Mo species concentration, and low N-K peak energy, the identification of Mo–N species was found to be rather challenging. The identification of Mo–N species was only possible in the case of 10-Mo–N/SiO_2 displaying the largest nitride particle size (2.9 ± 0.3 nm).

2.1.3. Surface Properties of Mo–N Supported Catalysts

The surface properties, chemical composition and oxidation states of elements, were investigated using X-ray photoelectron spectroscopy. To understand the evolution of the surface composition under the activation step, XPS spectra of the 10-Mo–O/supports obtained directly after the calcination step and the nitride 10-Mo–N/supports formed after the activation step were

Table 1. Textural properties of unsupported MoO_3 and supported Mo–O based materials after calcination.

	MoO_3[a] (wt%)	S_{BET}[b] ($m^2\ g^{-1}$)	S_μ[c] ($m^2\ g^{-1}$)	V_p[d] ($cm^3\ g^{-1}$)	D_p[e] (nm)	Mo Mean Particle Size (nm)[f]
MoO_3	–	4	–			–
10-Mo–O/Al_2O_3	10.7	208 (251)	— (10)	0.99 (1.00)	8.3 (8.2)	1.7 ± 0.1
10-Mo–O/CeO_2	11.8	194 (237)	— (—)	0.16 (0.16)	3.0 (3.1)	ND
10-Mo–O/SiO_2	10.8	262 (294)	— (24)	1.07 (0.92)	13.2 (13.8	2.9 ± 0.3
10-Mo–O/SBA-15	10.8	465 (760)	68 (131)	0.82 (1.1)	6.6 (6.5)	1.3 ± 0.3

[a] MoO_3 content measured by ICP–OES in the calcined samples.
[b] S_{BET} calculated by the BET method.
[c] S_μ microporous surface area.
[d] V_p total pore volume calculated using BJH method.
[e] D_p mean pore size calculated using BJH method; ND not detectable; properties of the supports are given in parentheses.
[f] Average of 50 particles counted for each sample.

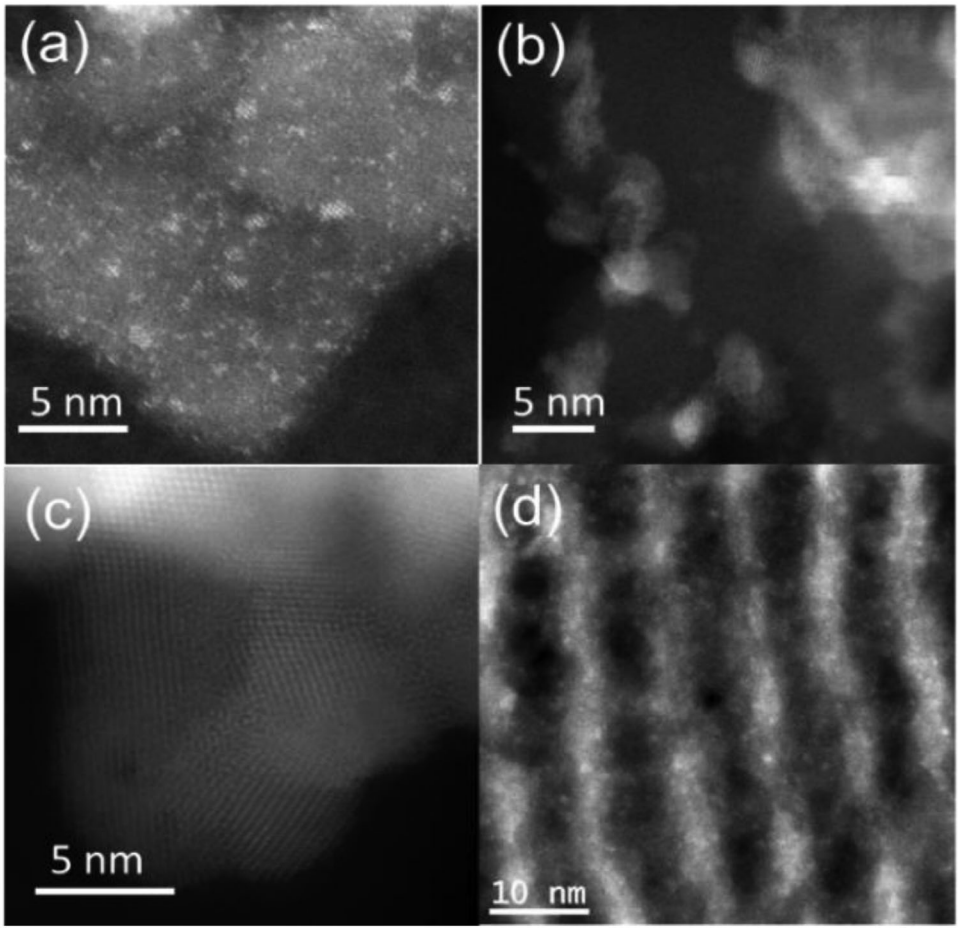

Figure 3. Representative HAADF images of (a) 10-Mo–N/Al_2O_3, (b) 10-Mo–N/SiO_2, (c) 10-Mo–N/CeO_2, and (d) 10-Mo–N/SBA-15.

acquired. The activation step was conducted in a pretreatment environmental chamber connected to the XPS (700 °C under 75 vol% H_2 in N_2 flow for 2 h), to avoid any contact of the sample with air and minimize surface contamination. The results are summarized in Figure 4; Figures S3 and S4; Table 2 and Tables S1–S3.

10-Mo–O/supports. The XPS spectra along with spectral decomposition of Mo 3d region for the calcined samples are presented in Figure 4a. All the supported oxides 10-Mo–O/Al_2O_3, 10-Mo–O/SiO_2, 10-Mo–O/SBA-15, and 10-Mo–O/CeO_2 displayed a similar Mo 3d XPS profile, characterized by two major spectral lines corresponding to Mo $3d_{5/2}$ and Mo $3d_{3/2}$ spin–orbit components, which correspond to a formal Mo^{6+} oxidation state.[16]

10-Mo–N/supports. Upon the activation step, at 700 °C under H_2/N_2 for 2 h, a shift to lower binding energies was observed in all the catalysts, indicating successful oxidation state reduction of Mo species. However, disparities in Mo 3d/Mo 3p binding

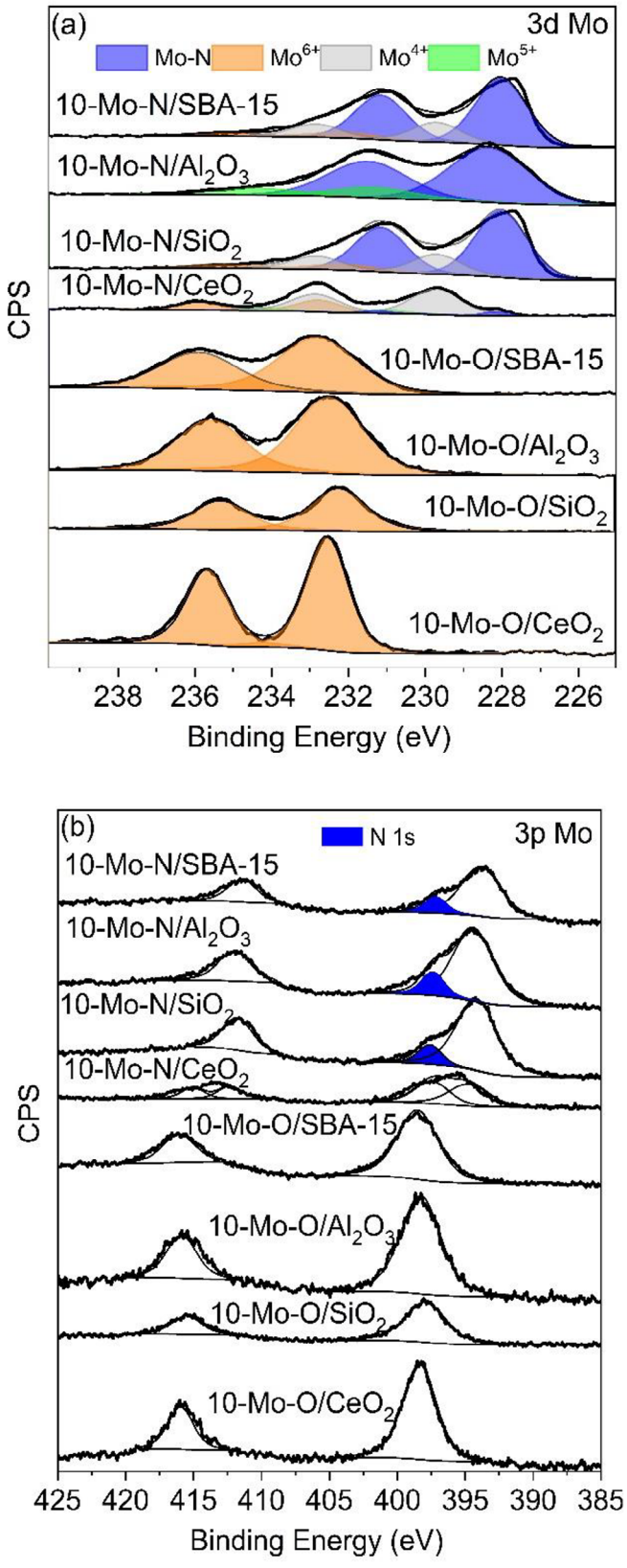

Figure 4. XPS spectra of solids before (10-Mo–O/support) and after nitridation step (10-Mo–N/support) in (a) Mo 3d region and (b) Mo 3p region.

energies are observed, pointing the impact of the nature of the support on the stabilization of different chemical environments of Mo species (Figure 4 and Table 2) compared to the profile of the bulk unsupported Mo_2N (Figure S4).

In the case of siliceous supports (SiO_2 and SBA-15), the high-resolution Mo 3d XPS profile can be decomposed into several peaks (Figure 4a). In both materials, the major contribution is related to the presence of Mo–N species with two major spectral lines at 228.4 eV and 231.5 eV.[17] Additional peaks correlated to the presence of Mo^{6+} and Mo^{4+} have been also observed in both catalysts. The surface composition of Mo species was found to be similar between SiO_2 and SBA-15, where in both catalysts, Mo–N species were predominant ~66.4% and ~69.7% in 10-Mo–N/SBA-15 and 10-Mo–N/SiO_2, respectively. Moreover, in both catalysts, at least 20 at.% of Mo species were present as Mo^{4+}. The remaining fraction of Mo species that was not reduced was estimated to be ~2.8 at.% of Mo^{6+} in SBA-15, and ~8.3 at.% of Mo^{6+} in SiO_2. Such results indicate that Mo–Si interaction affected the nitridation mechanism similarly in both amorphous SiO_2 and SBA-15. The comparable distribution of Mo species when supported in SiO_2 or in SBA-15 strongly suggests that confinement in SBA-15 has no discernible chemical effect on the nature of stabilized Mo–N species. In a similar manner, when 10-Mo–N/Al_2O_3 was subjected to the activation step, the surface was mainly populated with Mo–N species ~82.0%. Furthermore, the spectral decomposition of the high-resolution Mo 3d region revealed the presence of an important fraction of Mo species as Mo^{5+} ~18.0 at.%. Interestingly, when investigating 10-Mo–N/CeO_2, the spectral decomposition of Mo 3d XPS profile exhibited the predominance of Mo^{4+} species with Mo $3d_{5/2}$ and Mo $3d_{3/2}$ spin–orbit components of 229.7 eV and 232.8 eV. An additional set of peaks related to Mo^{6+}, Mo^{5+}, and Mo–N were also identified. The distribution of Mo oxides species was determined to be ~65.5 at.% for Mo^{4+}, ~25.6 at.% for Mo^{6+}, 7.4 at.% for Mo^{5+}, and only 4.5 at.% was found to be in the form of Mo–N. Such observations indicate that supporting Mo on CeO_2 increased the Mo^{4+} content at the expense of Mo–N formation.

The impact of the activation step on the support elements has also been examined by XPS (Figure S3). In the case of 10-Mo–O/Al_2O_3, the Al 2p XPS profile was fitted as a single peak at ~74.1 eV. This is due to the closely spaced Al 2p peak spin–orbit components. Upon the activation step, a slight shift of the Al 2p XPS profile to lower binding energies of 73.6 eV was observed. In the case of SiO_2, the Si 2p XPS profile was characterized by one peak as well with a binding energy of 103.2 eV and a slightly higher BE after nitridation at 104.0 eV (Table S2). In the case of SBA-15, both Si–O–Si and Si–OH corresponding peaks were identified in the Si 2p region, with BE of 104.0 eV and 103.2 eV, respectively. Upon the activation step, only a slight shift of Si–OH peak to lower binding energy of 103.5 eV was observed.

In the case of CeO_2, the Ce 3d core-level XPS spectrum (Figure S3) was decomposed into 10 gaussian peaks following the methodology proposed by Burroughs et. al.[18] Signals labeled as U, U″, U‴ and (V, V″, V‴) correspond to the $3d_{3/2}$ and ($3d_{5/2}$) final states of Ce^{4+}. Meanwhile, the peaks labeled as U′, U_o and (V′, V_o) refer to the $3d_{3/2}$ and ($3d_{5/2}$) final states of Ce^{3+}.

Table 2. Position of 3d Mo peaks of unsupported and supported Mo-based catalysts before and after nitridation and element surface composition.

	Mo Peaks B.E. (eV)								Surface Composition (at.%)			
	Mo^{6+}		Mo^{5+}		Mo^{4+}		Mo–N		Mo^{6+}	Mo^{5+}	Mo^{4+}	Mo–N
	$3d_{5/2}$	$3d_{3/2}$	$3d_{5/2}$	$3d_{3/2}$	$3d_{5/2}$	$3d_{3/2}$	$3d_{5/2}$	$3d_{3/2}$				
10-Mo–N/SBA-15[a)]	232.3	235.4	–	–	230.0	233.2	228.4	231.5	12.8	–	20.8	66.4
10-Mo–N/Al_2O_3[a)]	–	–	231.3	234.5	–	–	228.3	231.5	–	18.0	–	82.0
10-Mo–N/SiO_2[a)]	232.1	235.2	–	–	229.7	232.8	228.0	231.1	8.3	–	22.1	69.7
10-Mo–N/CeO_2[a)]	232.76	235.9	231.0	234.1	229.7	232.8	228.1	231.3	25.6	7.4	65.5	4.5
10-Mo–O/SBA-15	232.8	235.9	–	–	–	–	–	–	100	–	–	–
10-Mo–O/Al_2O_3	232.5	235.6	–	–	–	–	–	–	100.0	–	–	–
10-Mo–O/SiO_2	232.2	235.3	–	–	–	–	–	–	100.0	–	–	–
10-Mo–O/CeO_2	232.6	235.7	–	–	–	–	–	–	100.0	–	–	–

[a)] Catalyst subject to pretreatment under reaction condition at 700 °C for 2 h (3:1 H2/N2 50 mL/min) in environmental activation chamber connected to XPS before analysis.

For the 10-Mo–O/CeO_2, only Ce^{4+} species are present with their corresponding binding energies of 901.3 eV (882.7 eV), 907.2 eV (888.7 eV), and 916.7 eV (898.2 eV) for U (V), U″ (V″), and U‴ (V‴), respectively. After pretreatment step, a shift to lower binding energies is observed, confirming the partial reduction of Ce^{4+} to Ce^{3+}. The newly formed Ce^{3+} displayed BE for U′, U_o and (V′, V_o) at 903.9 eV, 899.5 eV (885.4 eV, 881.0 eV).

2.1.4. EPR Studies

The process of Mo nitridation during the activation step has been further investigated by EPR. Prior to the activation step, all the Mo–O supported materials are EPR silent due to the absence of paramagnetic centers as Mo is present in the +6 oxidation state. Upon activation, Mo displayed a range of oxidation states. However, only Mo^{5+} is paramagnetic and can yield an EPR signal (Figure 5). The EPR spectra recorded, after the activation step, for the 10-Mo–N/Al_2O_3 displayed a strong Mo^{5+} signal with an isotropic line centered at a g value of 1.95 (Figure 5a). The kinetic evolution of Mo^{5+} species during the activation step was also studied by in situ EPR (at 700 °C under 3:1 H_2/N_2 for 2 h). The reduction leads to a sharp increase in the formation of Mo^{5+} that reached a plateau after 40 mins of pretreatment (Figure 5c). The reduction process was accompanied by an initial increase in the concentration of anionic vacancies where the signal then rapidly disappears as the temperature increases. To have information about the local structure of Mo^{5+} in the case of 10-Mo–N/Al_2O_3, a HYSCORE experiment at 5 K (Figure 6) was performed. On this HYSCORE spectrum, one can observe in the weak coupling quadrant the presence of a signal centered at 3.9 MHz, resulting from the interaction of an aluminum weakly coupled by dipolar mechanism. In the strong coupling quadrant, we observe four peaks of correlations in the antidiagonal separated by two times the Larmor frequency of Al (7.8 MHz). This profile indicates the presence of two strongly coupled aluminum via Mo–O–Al covalent bonds with respective A_{iso} coupling constants of 15 and 16 MHz. Therefore, these EPR results indicate that the formation of Mo^{5+} species is a bulk phenomenon.

After the activation of MoO_x supported over CeO_2, the recorded EPR spectrum indicated the presence of Mo^{5+} (Figure 5a). In this case, the EPR signal was anisotropic with a square plane symmetry ($g_z = 1.97$ and $g_{x,y} = 1.95$). During the kinetic studies at 700 °C, the reduction/nitridation process was characterized by an increase in the concentration of Mo^{5+} species, accompanied with an increase of anionic vacancies concentration reaching a maximum at 10 min and gradually decreasing afterward to stabilize after 60 min of pretreatment (Figure 5c,d).

Finally, when Mo is supported on siliceous-based supports, only a weak isotropic Mo^{5+} signal with a g factor of 1.94 is observed (Figure 5a). During the kinetic evolution at 700 °C under H_2/N_2, this signal quickly disappears, indicating the loss of Mo^{5+}, leaving only a weak signal related to the presence of oxygen vacancies (Figure 5d). The remaining Mo^{5+} species seem to be marginal after the nitridation step for silica-supported catalysts based on EPR results, which is in accordance with XPS results that demonstrated $a > 64\%$ of nitridation over silica-supported catalysts.

2.1.5. Effect of Mo-Supported Interactions on Mo Reducibility and Affinity Toward Hydrogen

The effect of the nature of the support on the reduction kinetics of Mo oxides was evaluated by means of H_2-TPR measurements and the results are compared to those collected for the unsupported α-MoO_3. The results are presented in Figure 7 and Table S5. TPR profiles of supported Mo oxides are compared to the unsupported α-MoO_3, where significant changes in the reduction process are observed. The reduction profile of unsupported α-MoO_3 proceeds via two steps as previously seen in the literature (Figure S5-a). First the reduction of α-MoO_3 into MoO_2 occurs, and the process is characterized by a sharp hydrogen consumption peak at 770 °C. It is followed by the reduction of MoO_2 into metallic Mo at higher temperatures.[19] During the reduction process, the formation of intermediate species such as Mo_4O_{11} has also been reported in the literature.[19] However, the reduction of MoO_2 was not entirely complete even at temper-

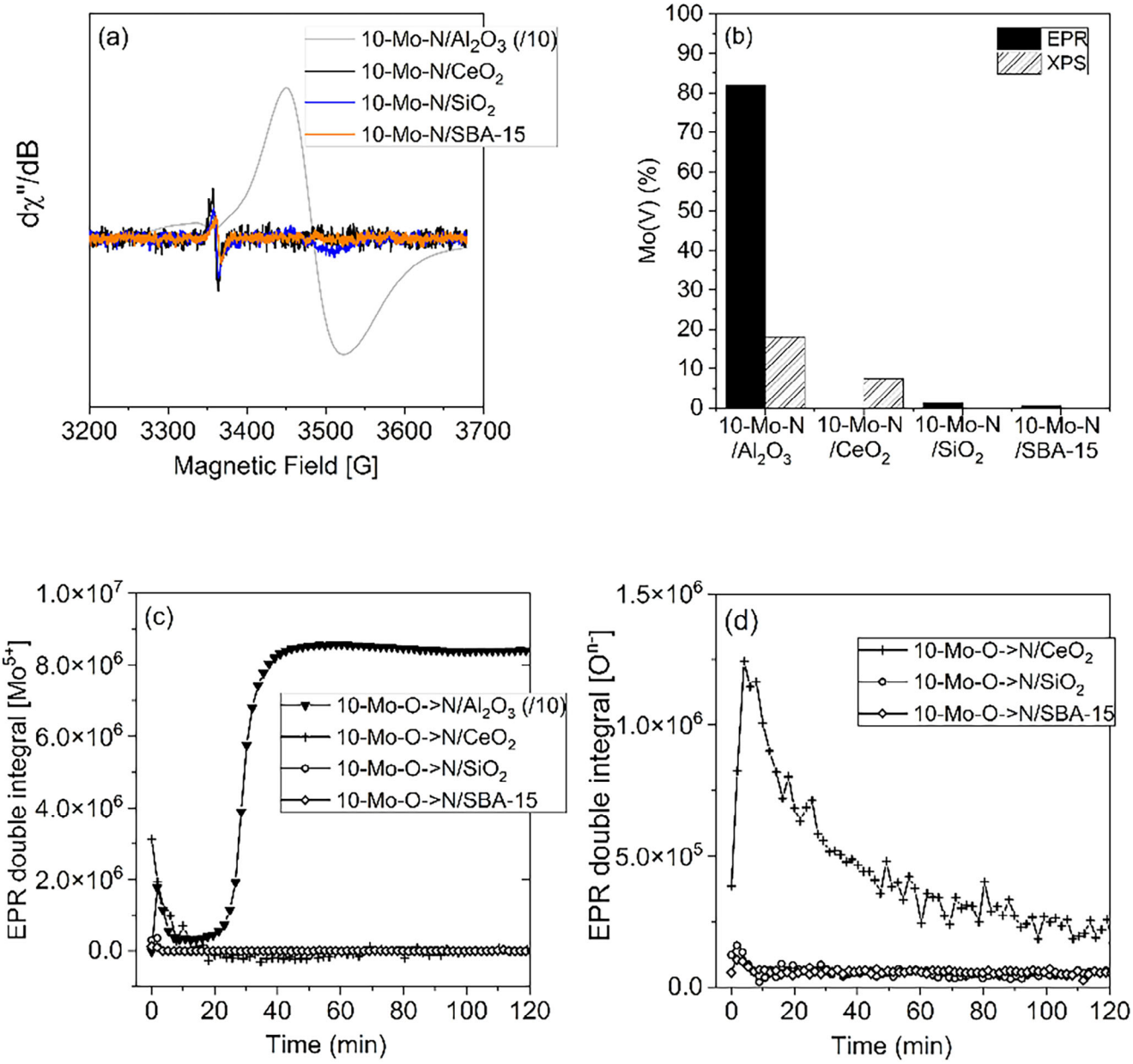

Figure 5. (a) EPR spectra registered for the catalysts after pretreatment at 700 °C under H_2/N_2, (b) fraction of Mo^{5+} after pretreatment conditions by EPR and XPS, (c) kinetic evolution of Mo^{5+} species at 700 °C under H_2/N_2, and (d) kinetic evolution of O^{n-} species at 700 °C under H_2/N_2.

atures as high as 1000 °C. Based on the H_2 quantity consumed, a Mo(VI) reduction degree of 89% is obtained. In the case of all supported catalysts, the reduction process started at lower temperatures with respect to α-MoO_3. Depending on the nature of the support, the temperature of the first maximum reduction domain shifted to lower temperatures, with the following order: 10-Mo–O/Al_2O_3 (˜447 °C) < 10-Mo–O/CeO_2 (˜515 °C) < 10-Mo–O/SBA-15 (˜530 °C) < 10-Mo–O/SiO_2 (˜565 °C) < α-MoO_3 (˜770 °C). In a similar manner, the temperature of the second reduction peak associated with the formation of metallic Mo shifted to lower temperatures with slight differences observed between the different supports. In 10-Mo–O/CeO_2, the second reduction event was characterized by a broad and small reduction peak observed between 600 and 800 °C, denoting the stabilization of Mo-oxide intermediates.

Furthermore, a third reduction process starting at temperatures as high as 880 °C was observed. This might be related to the reduction of CeO_2 bulk species at higher temperatures and/or reduction of Mo species in strong interaction with the support. For comparison, the H_2-TPR profiles of the bare supports are presented in Figure S4b and as expected only CeO_2 displayed redox properties. The H_2-TPR profile was characterized by two peaks with temperatures of reduction maxima at ~450 °C and ~790 °C. The first peak has been assigned to the reduction of superficial CeO_x species, whereas the second peak has been correlated to the reduction of bulk CeO_2 species, respectively.[20]

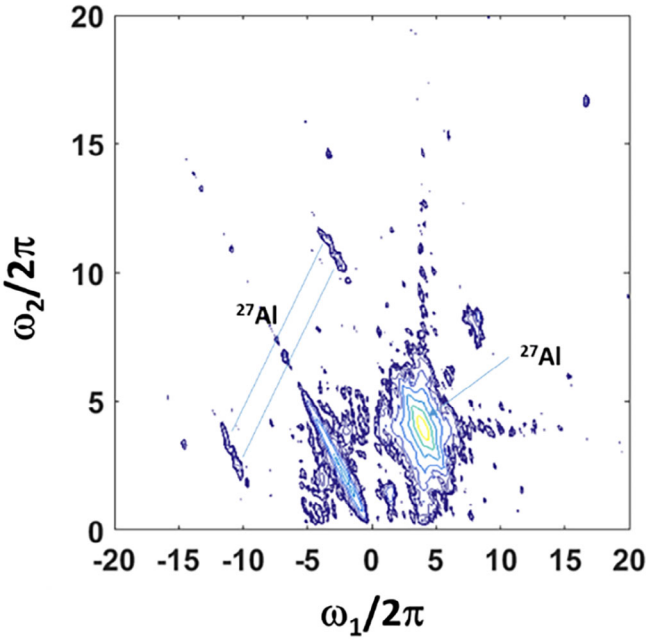

Figure 6. 2D-HYSCORE of nuclear interaction for 10-Mo–N/Al_2O_3.

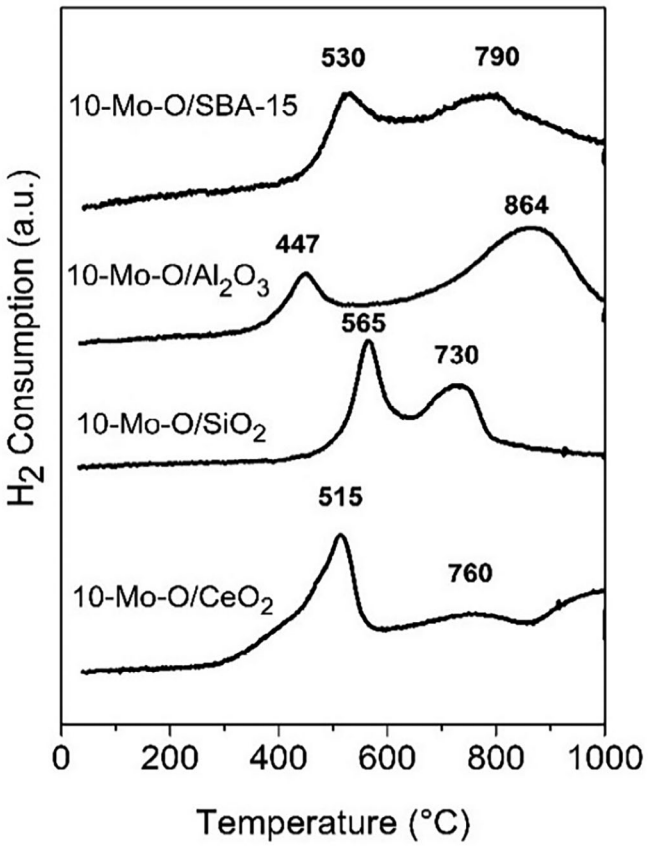

Figure 7. H_2-TPR profiles of 10-Mo–O/Al_2O_3, 10-Mo–O/SiO_2, 10-Mo–O/CeO_2, and 10-Mo–O/SBA-15.

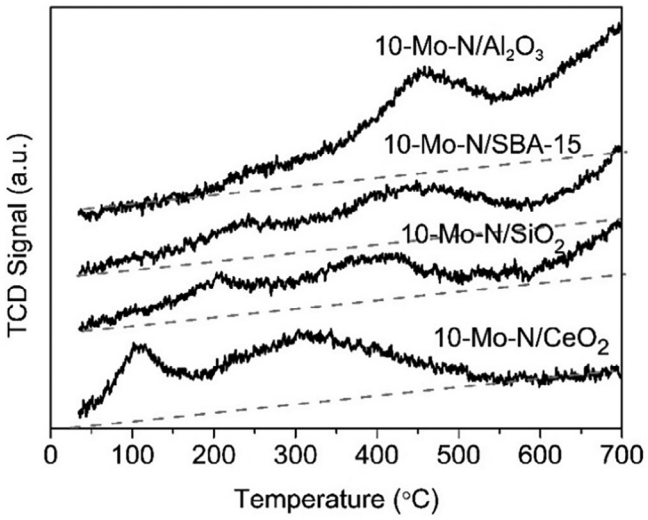

Figure 8. H_2-TPD profiles of 10-Mo–N/Al_2O_3, 10-Mo–N/SiO_2, 10-Mo–N/SBA-15, and 10-Mo–N/CeO_2.

The temperature of the second maximum reduction peak was also fairly high on 10-Mo–O/Al_2O_3 (~864 °C), especially when compared to Mo–O supported on siliceous supports (10-Mo–O/SiO_2 at ~730 °C and 10-Mo–O/SBA-15 at ~790 °C). Furthermore, small differences in Mo oxides reducibility were also observed between SiO_2 and SBA-15. As mentioned above, the reduction process started earlier in 10-Mo–O/SBA-15 when compared to 10-Mo–O/SiO_2, signifying that particle size has a role in influencing the reduction behavior of Mo oxides species. In summary, the reactivity of Mo oxides species towards hydrogen was greatly impacted by the nature of the support and particle size.

The effect of Mo-support interaction on the activation of H_2 was studied by means of H_2-temperature programmed desorption (Figure 8). Starting with alumina, the H_2-TPD profile of 10-Mo–N/Al_2O_3 was characterized by two desorption peaks, the first peak being in the range of 350–550 °C and the second desorption peak starting from 550 °C. When Mo is supported on siliceous supports, similar H_2-TPD profiles are observed for SBA-15 and SiO_2. The corresponding H_2-TPD profiles were characterized by three desorption peaks. The first one starting from 100 to 300 °C, the second desorption peak from 350 to 550 °C, and a third desorption peak at high temperature (>550 °C). Small disparities between the two desorption profiles are, however, observed especially when the temperatures of the maximum desorption are compared, which are slightly shifted to higher temperatures in the case of 10-Mo–N/SBA-15. As shown in Figure 8, the desorption profile of 10-Mo–N/CeO_2 was characterized by a first desorption peak at low temperature between 50 and 150 °C, which can be related to the desorption of H_2 adsorbed on the unsaturated sites from $CeO_{2-\delta}$ surface.[21] A second broad H_2-desorption peak is observed at temperatures ranging between 150 and 550 °C. Surprisingly, no H_2 desorption was observed at higher temperatures. The differences in H_2-TPD profiles reveal the coexistence of different possible H_2 adsorption sites, with each support displaying different Mo species population (Mo–N, Mo^{6+}, Mo^{5+}, and Mo^{4+}) after the activation steps

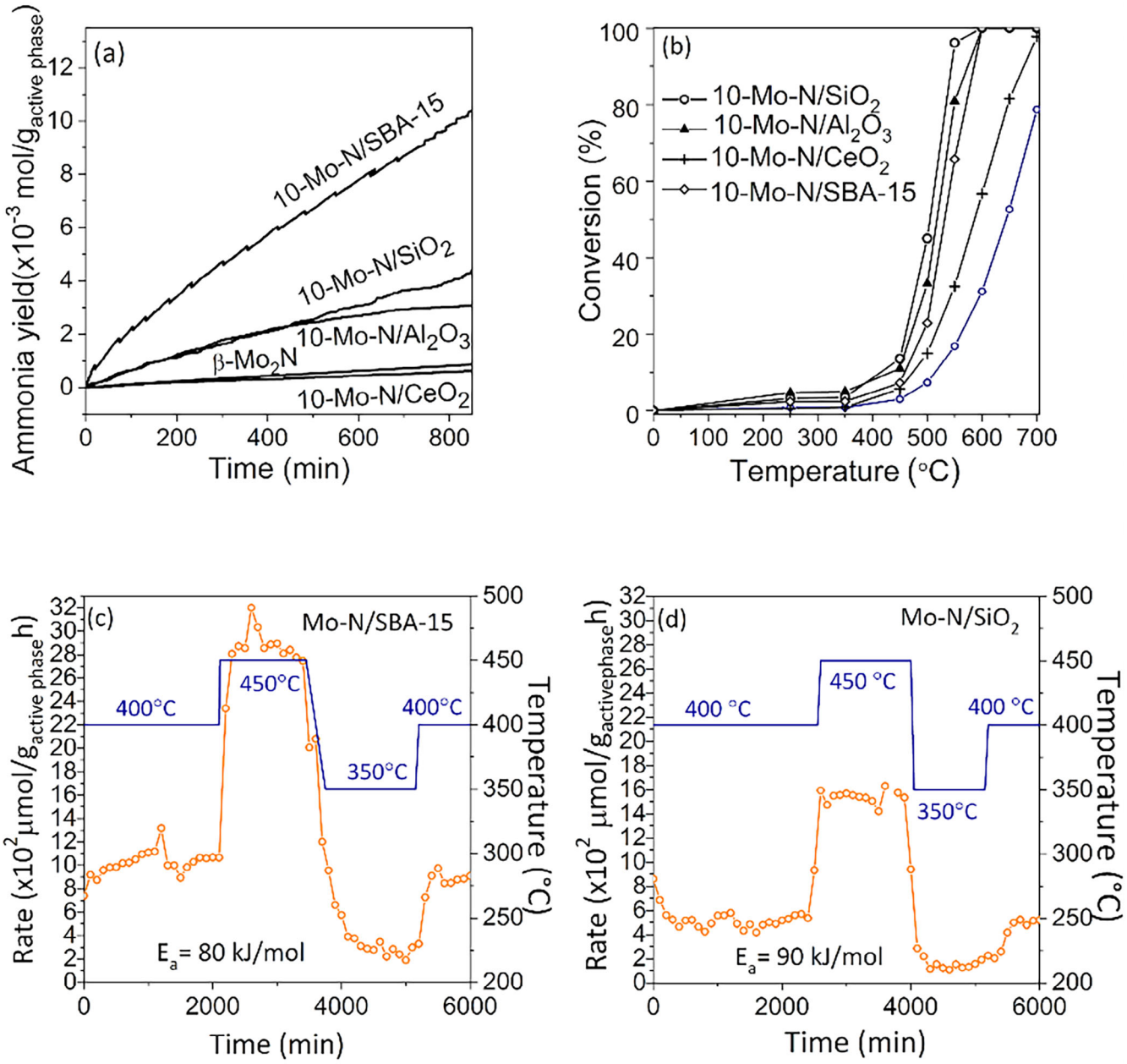

Figure 9. Catalytic activity of 10-Mo–N/Al_2O_3, 10-Mo–N/SiO_2, and 10-Mo–N/CeO_2 for (a) ammonia synthesis at 400 °C and (b) ammonia decomposition from 250 to 700 °C. (c) Catalytic activity and stability of 10-Mo–N/SBA-15 and (d) catalytic activity and stability 10-Mo–N/SiO_2 for ammonia synthesis at 400 °C, 450 °C, and 350 °C.

and eventually contributing to the adsorption of H_2 (case of CeO_2).

2.2. Performance in NH_3 Synthesis–Decomposition

The catalytic activity of Mo supported catalysts was evaluated in ammonia synthesis and ammonia decomposition (Figure 9 and Table 3). Control tests were performed prior to the catalytic tests to ensure that the empty reactor and bare supports show no activity. As a general comment, the rates presented, whatever the catalyst, are far below the thermodynamic limits under the operational conditions. Thus, the trends for synthesis and decomposition reflect the inherent differences in catalyst reaction kinetics and not reaction thermodynamics.

2.2.1. Ammonia Synthesis

The catalytic activity of Mo–N supported catalysts in ammonia synthesis was evaluated at a weight hourly space velocity (WHSV) of 18 000 mL g^{-1} h^{-1} at 400 °C and at ambient pressure (Figure 9a). When compared to the unsupported β-Mo_2N (initial rate of 76 μmol $g_{catalyst}^{-1}$ h^{-1}), only 10-Mo–N/SBA-15 catalyst (initial rate of ~85 μmol $g_{catalyst}^{-1}$ h^{-1}) displayed a higher catalytic activity for ammonia synthesis. Under the

Table 3. Summary of the catalytic activity of supported Mo–N supported catalysts in ammonia synthesis and ammonia decomposition.

	Ammonia Synthesis			Ammonia Decomposition		
	Initial Rate (μmol $g_{catalyst}^{-1}$ h^{-1})	Initial Rate (μmol $g_{active\ phase}^{-1}$ h^{-1})[a)]	Steady State Rate** (μmol $g_{catalyst}^{-1}$ h^{-1})	T_{10}	T_{100}	E_a (kJ mol^{-1})
β-Mo_2N	76	76	77	–	–	–
10-Mo–N/SBA-15	85	1208	51	460	585	71
10-Mo–N/SiO_2	34	481	34	425	560	71
10-Mo–N/Al_2O_3	26	372	0	450	575	59
10-Mo–N/CeO_2	ND[b)]	ND	ND	470	–	78

[a)] Rate normalized to the theoretical Mo_2N content in the catalysts, considering a complete conversion of MoO_3 to Mo_2N.
[b)] ND: not detected, **steady state rate calculated after 5 h of reaction.

same catalytic conditions, the 10-Mo–N/SiO_2 (initial rate of ~34 μmol $g_{catalyst}^{-1}$ h^{-1}) exhibited lower catalytic activity than those observed for β-Mo_2N phase and 10-Mo–N/SBA-15. When normalized against the active phase loading, an initial rate of ~1208 μmol $g_{active\ phase}^{-1}$ h^{-1} and ~481 μmol $g_{active\ phase}^{-1}$ h^{-1} is obtained over 10-Mo–N/SBA-15 and 10-Mo–N/SiO_2, respectively. Although 10-Mo–N/SiO_2 catalyst did not show any sign of deactivation over time of reaction, the 10-Mo–N/SBA-15 on the other hand showed a slight deactivation during the first hour of reaction, to stabilize at a constant production rate of 51 μmol $g_{catalyst}^{-1}$ h^{-1}, which is 60% above the stable rate obtained for 10-Mo–N/SiO_2 catalyst (Table 3). In 10-Mo–N/Al_2O_3, the initial ammonia synthesis rate was found to be 26 μmol $g_{catalyst}^{-1}$ h^{-1}, denoting a decrease in the catalytic activity when the active phase is supported on Al_2O_3 with respect to SBA-15 and SiO_2. Furthermore, the catalytic activity of 10-Mo–N/Al_2O_3 was found to decrease gradually with time until completely deactivating after 10 h of reaction. Finally, the 10-Mo–N/CeO_2 sample did not display any catalytic activity in ammonia synthesis despite the formation of small Mo nanoparticle species.

2.2.2. Stability of Mo–N Nanoparticles on Siliceous Supports

Stability tests have been performed for both Mo–N/SiO_2 and Mo–N/SBA-15 at different temperatures (400 °C, 450 °C, and 350 °C) for 100 h (Figure 9c,d). The results confirm that both catalysts were stable under reaction conditions at different temperatures. The effect of particle size and dispersion is evident in SBA-15, where enhanced activity is observed compared to Mo–N supported on commercial silica. The average rates for ammonia production for Mo–N/SBA-15 were 1029, 2881, and 296 μmol $g_{active\ phase}^{-1}$ h^{-1} at 400 °C, 450 °C and 350 °C, respectively, whereas the rates for Mo–N/SiO_2 were 508, 1542, and 140 μmol $g_{active\ phase}^{-1}$ h^{-1} at 400 °C, 450 °C, and 350 °C, respectively The activation energies were also calculated and found to be around 80 kJ/mol for Mo–N/SBA-15 and 90 kJ/mol for Mo–N/SiO_2.

2.2.3. Ammonia Decomposition

The effect of the nature of the support in tuning the catalytic activity of Mo species in ammonia decomposition was also studied and the results are shown in Figure 9b and in Table 3. As expected, depending on the nature of the support, differences in the catalytic activity of Mo species are observed. However, all the studied catalysts were found to be active in ammonia decomposition. At low temperatures, the order of activity, classified as a function of 10% NH_3 conversion temperature, is: 10-Mo–N/SiO_2 (425 °C) < 10-Mo–N/Al_2O_3 (450 °C) < 10-Mo–N/SBA-15 (460 °C) < 10-Mo–N/CeO_2 (470 °C). At higher temperatures, complete conversion of NH_3 was achieved in the following order: 10-Mo–N/SiO_2 (560 °C) < 10-Mo–N/Al_2O_3 (575 °C) < 10-Mo–N/SBA-15 (585 °C) < 10-Mo–N/CeO_2 (~700 °C). These results imply that the nature of the support was not altering severely the catalytic activity of Mo species in ammonia decomposition as was the case in ammonia synthesis. Surprisingly, by a comparison between the siliceous supports, the catalytic activity seems to be favored by the increase in Mo species particle size.

3. Discussion

Despite achieving high dispersion of Mo species and small particle size in all the catalysts, large disparities in the catalytic activity in ammonia synthesis were observed, where the catalysts supported on silica were better performing and more stable. On the contrary, complete deactivation of 10-Mo–N/Al_2O_3 after 10 h of reaction is observed, and 10-Mo–N/CeO_2 displayed no catalytic activity, suggesting an important role of the support in modulating the final state of the Mo phase. To probe the origin of the catalytic activity differences, the surface composition was studied by means of XPS. Before the activation step, Mo^{6+} was the predominant species in all the supported 10-Mo–O/support materials. However, upon nitridation and depending on the nature of the support, various oxidation states were detected. Over siliceous-based supports, the catalysts showed similar XPS profiles where most of Mo–O species were converted successfully to Mo–N in both catalysts. This stands to show that the nitridation mechanism remained unchanged when switching between two supports of the same nature. A high level of nitridation was also reported for the alumina supported catalyst for which Mo–N species were quantified at 82.0 at.% alongside Mo^{5+} (18.0 at.%). Surprisingly, the distribution of Mo species was found to be quite different in 10-Mo–N/CeO_2 where only a small fraction of Mo species was nitrided, 4.5 at.%; after the activa-

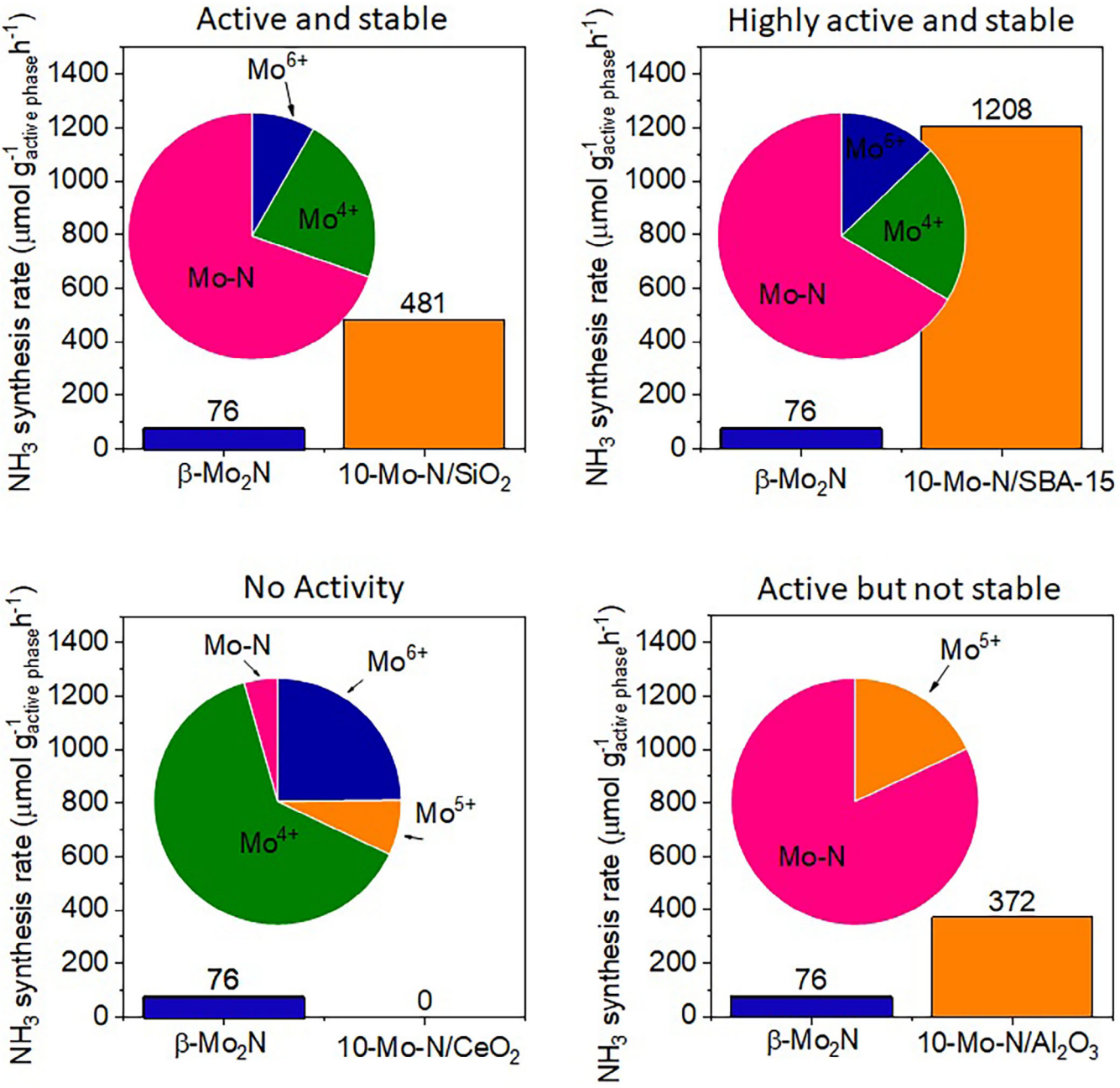

Figure 10. Impact of support identity on the chemical composition and performance of supported molybdenum nitrides in ammonia synthesis. Note: 10-Mo–N/CeO_2 sample: proportion of Mo^{5+} issued from XPS.

tion step, Mo species predominantly formed are Mo^{4+} (65.5 at.%), Mo^{6+} (25.6 at.%), and to a lesser extent Mo^{5+} (7.4 at.%). The stabilization of Mo oxides species when supported on CeO_2 might explain the absence of catalytic activity of 10-Mo–N/CeO_2 catalyst in ammonia synthesis. The differences in the catalytic behavior cannot be solely explained by the differences in Mo–N species concentration (Figure 10). 10-Mo–N/Al_2O_3 displayed the highest surface concentration of Mo–N species but displayed lower catalytic activity and poor stability as a function of time, leading to a complete deactivation measured after only 10 h of reaction. The catalytic activity of Mo–N species was found to be dependent to crystallographic phases formed (i.e., β-Mo_2N and δ-MoN)[14] and degree of nitridation (δ-MoN).[14,22] Furthermore, the hydrogen chemisorption capacity of Mo–N species were observed to be influenced by several factors such as chemical composition ($Mo^{\delta+}$/N ratio), Mo oxidation states, and nitrogen-deficient site density,[23] and the mechanism of MoO_3 nitridation is sensitive to several parameters (particle size, support, gas composition, space velocity):[24]

(i) nitridation of MoO_3 to β-Mo_2N proceeds through initial reduction to MoO_2, further nitrided to MoN_x (without formation of Mo(V) species).[23,25]

(ii) γ-Mo_2N forms through molybdenum bronze ($H_xMo_x^{5+}Mo_{1-x}^{6+}O_3$) as an intermediate species before nitridation.[24a]

Thus, the formation of a specific Mo–N phase can be modified by an appropriate control of the nitridation conditions[26] and/or by controlling the Mo-support interaction. Based on the results obtained, the nitridation process was observed to be significantly different in the case of 10-Mo–N/Al_2O_3 catalyst where large quantity of Mo^{5+} species was detected. The concentration of Mo^{5+} increased with time of reduction to reach a plateau after 40 min of nitridation. In these conditions, the formation of hydrogen molybdenum bronze ($H_xMo_x^{5+}Mo_{1-x}^{6+}O_3$) intermediates is likely. Another hypothesis could be the formation of $Al_2(MoO_4)_3$, as suggested by XPS with a BE ~73.6 eV corresponding to Mo–O-Al, hosting the pentavalent Mo.[27] This formation is not inconsistent with the absence of crystalline aluminum molybdate phase by XRD, considering the limited sensibility of the technique (poor crystallinity, small clusters), and finally the limited proportion of Mo involved in the aluminum molybdate phase. Thus, it is more likely, that a part of the Mo species is located in the aluminum–molybdate extra phase, associated to the reactivity of hydroxylated surface of transition alumina, which might explain the low initial activity rate of 10-Mo–N/Al_2O_3 (26 μmol $g_{catalyst}^{-1}$ h^{-1}) when compared to 10-Mo–N/SBA-15 (84 μmol $g_{catalyst}^{-1}$ h^{-1}). The progressive formation of $Al_2(MoO_4)_3$, might be also responsible for the deactivation of the catalyst.[28] In contrast with 10-Mo–N/Al_2O_3, only a weak isotropic Mo^{5+} signal is observed for silica-based catalysts, which rapidly disappeared during the activation step of Mo species. It indicates that the process of nitridation is rather dominated by direct reduction of Mo^{6+} to Mo^{4+} without massive Mo^{5+} intermediate formation. Part of the discrepancies in the catalytic activity might be explained by the differences of Mo-species populating the surface.

The example of 10-Mo–N/CeO_2 showcased the role of CeO_2 in stabilizing MoO_x species and slowing down the nitridation process, leading to an inactive catalytic material under the same conditions of activation used for silica and alumina supported catalysts. However, modification of activation conditions (i.e., higher reduction temperature for ceria reduction) could be envisaged to modify electron transfer ability of the support and improve Mo phase nitridation.

4. Conclusion

The preparation of supported nitride phases offers an elegant approach for the preparation of small Mo–N nanoparticles with good performances for ammonia synthesis and ammonia decomposition. The results of characterizations confirmed the high dispersion of Mo species within the different supports (namely a commercial SiO_2 and a mesostructured SBA-15 silica, commercial Al_2O_3 and CeO_2). However, the performance and stability of Mo–N supported catalysts was found to be largely dependent on the nature of the supports. An initial rate of ~1208, ~481, and ~372 μmol $g_{active\ phase}^{-1}$ h^{-1} is obtained over 10-Mo–N/SBA-15, 10-Mo–N/SiO_2 and 10-Mo–N/Al_2O_3 catalysts, respectively, whereas 10-Mo–N/CeO_2 did not express any catalytic activity. Furthermore, 10-Mo–N/Al_2O_3 deactivated after few hours of reaction, whereas catalysts supported over silica are far more stable with time. XPS analysis and EPR revealed that the identity and distribution of Mo (Mo–N, Mo^{6+}, Mo^{5+}, Mo^{4+},) species formed during the activation process were significantly influenced by the nature of the support. For instance, when supported on CeO_2, Mo species were predominantly stabilized in the oxidic forms and only a small fraction was found to be nitrided upon the activation step. The low concentration of Mo–N species in of 10-Mo–N/CeO_2 resulted in very low catalytic activity in ammonia synthesis. Despite the large gap in the catalytic behavior of Mo when supported on siliceous supports (SBA-15 and SiO_2) or on Al_2O_3, XPS analysis confirmed the successful nitridation of Mo species during the activation step on both types of supports. However, in situ EPR revealed that the process of nitridation of Mo species followed a different path depending on the nature of the support. The catalytic activity of Mo species in ammonia decomposition was also investigated, revealing variations in activity depending on the nature of the support. Nonetheless, all studied catalysts were active in ammonia decomposition. At both low and high temperatures, the order of activity differed across supports, with 10-Mo–N/SiO_2 showing the highest activity. These results demonstrate the prominent role of the identity of the support in tuning the properties of the active sites and thus impacting the performance of Mo species in the catalytic activity.

5. Methodology

5.1. Catalyst Preparation

5.1.1. Chemicals

The following chemicals and commercial supports were purchased and used with no further purification: ammonium paraheptamolybdate tetrahydrate ($(NH_4)_6Mo_7O_{24}.4H_2O$, 99 wt%, Alfa Aesar), SiO_2 (Saint-Gobain NORPRO SS61138), Al_2O_3 (Saint-Gobain NORPRO SA6176), and CeO_2 (Solvay ECL15).

5.1.2. Mo–N Supported Catalyst

Mesoporous SBA-15 support was produced by hydrothermal method, under acidic conditions as described elsewhere.[29] The available commercial supports (i.e., Al_2O_3, SiO_2, and CeO_2) were utilized without prior treatment.

Supported molybdenum oxides were prepared by incipient wetness impregnation (IWI) method. In this procedure, the required weight of Mo precursor ($(NH_4)_6Mo_7O_{24}.4H_2O$, Aesar) was first dissolved in a volume corresponding to the pore volume of the respective support and then mixed with the support. The resulting mixture was aged during 5 days at 25 °C and then calcined at 400 °C with a heating rate of 1.5 °C min^{-1} for 5 h. All the

samples underwent a calcination step at 400 °C, 1.5 °C min^{-1}, for 5 h to form MoO_3 oxide phase. The nitridation process was conducted prior to catalytic reaction, during the pretreatment step, at 700 °C under a 75 vol% H_2/N_2 (BOC, 99.98%) gas mixture at a total gas flow of 60 mL min^{-1} for 2 h.

Herein, the samples obtained after the calcination step are denoted 10-Mo–O/support. The catalysts obtained after the pretreatment step are referred to as 10-Mo–N/support, and the post reaction samples as 10-Mo–N-PR/support, where *X* is the wt% of α-MoO_3 ($X = 10$ wt%).

5.2. Catalyst Characterization

5.2.1. X-ray Diffraction (XRD)

Powder X-ray diffraction (XRD) of the calcined and postreaction samples was performed using a Bruker X-ray AXS D8 Advance diffractometer in Bragg–Brentano geometry configuration fitted with a LynxEye Super Speed detector. XRD patterns were recorded with a Cu Kα radiation ($\lambda = 0.154$ nm, 40 kV, 30 mA) over a range of 10–80° and a scan rate of 0.02°/step and scan time of 0.5 s/step. Crystal phase identification was made by comparison with the ICDD database.

5.2.2. Inductively Coupled Plasma–Optical Emission Spectrometer (ICP–OES)

Prior to analysis, the catalysts were dissolved in a diluted mixture of HF–HCl and heated under microwave until complete dissolution. The concentration of Mo was determined using sequential scanning inductively coupled plasma with an optical emission spectrometer (Perkin Elmer Optima 2000 DV).

5.2.3. Elemental Analysis

The nitrogen content of the post reaction samples was determined by an elemental analyzer Vario Cube.

5.2.4. Nitrogen Physisorption

Surface areas and textural properties were determined by nitrogen physisorption using a Micromeritics Tristar II automated gas sorption system at the boiling temperature of liquid nitrogen. Before analysis, the samples were outgassed under dynamic vacuum at 300 °C for 3 h. Specific surface area and pore volume were then determined by the multipoint Brunauer-Emmett-Teller plot (BET) and by the Barrett, Joyner, and Halenda (BJH) method. The total pore volume (V_{pore}) was determined on the adsorption branch at $P/P_0 = 0.97$, whereas the micropore volume (V_{micro}) was determined by the *t*-plot method.

5.2.5. X-ray Photoelectron Spectroscopy (XPS)

XPS spectra were recorded on a Kratos Analytical AXIS Ultra DLD spectrometer employing a monochromatic Al Kα X-ray radiation (1486.6 eV), with an electron analyzer operating in a fixed pass energy of 20 eV. Binding Energies (BE) were calibrated to the C—C bonding signal in the C 1s core level at 284.8 eV. A pretreatment environmental activation chamber was used to mimic the catalytic pretreatment prior to analysis at 700 °C for 2 h under a 60 mL min^{-1} flow of 75 vol% H_2/N_2. The results were fitted using CasaXPS V2.3.24 software.

5.2.6. Transition Electron Microscopy (TEM)

Morphology analysis was performed using a TITAN Themis 300 S/TEM equipped with a high brightness Schottky field emission gun, a monochromator, and a probe aberration corrector, allowing energy and special resolution of approximately 150 meV and 70 pm, respectively. The microscope is equipped with annular dark field detectors and a super-X detector system comprising four windowless silicon drift detectors for electron dispersive x-ray spectroscopy (EDS). The experiments were conducted at 300 kV with a semiconvergence angle of ~20 mrad, a probe size of ~500 pm, and probe current between 60 and 100 pA. For high angle annular dark field (HAADF) imaging, the collection angles ranged from 50 to 200 mrad. EDS mapping was obtained using spectrum imaging mode with dwell time of 15 ms per pixel and continuously scanning frames until total acquisition time of about 15–20 minutes. For analysis, the samples were deposited on a 200-mesh lacey carbon.

5.2.7. Continuous Wave Electron Paramagnetic Resonance Measurement (CW EPR)

CW EPR experiments were recorded a Bruker high temperature resonator. The experiments were carried out at a frequency of 9.5 GHz with a modulation amplitude of 1 G and a microwave power of 5 mW. For kinetics study, the EPR experiment were conducted at 700 °C, under 75 vol% H_2/N_2, where the spectra were collected for 2 h with a spectrum recorded each 40 s. The quantification of Mo^{5+} is related to the pure Mo^{5+} reference. The Mo^{5+} proportion is calculated by the ratio of double integral of EPR signal normalized by the weight of analyzed sample.

5.2.8. Redox Properties

H_2-temperature programmed reduction (H_2-TPR) was performed in an Autochem chemisorption instrument (Micromeritics) equipped with a TCD for analysis. After an initial pretreatment step at 200 °C (under 50 mL min^{-1} of synthetic air, heating rate of 5 °C min^{-1}, 30 min), H_2-TPR experiments were performed from 25 to 1000 °C under 50 mL min^{-1} of 5.0 vol% H_2 in Ar (heating rate of 5 °C min^{-1}).

5.2.9. Hydrogen Chemical Adsorption

H_2-temperature programmed desorption (H_2-TPD) was conducted in an Autochem chemisorption instrument (Micromeritics) equipped with a TCD. In a typical test, 0.5 g of Mo–O/support was added to the reactor and pretreated under 75 vol% H_2 in N_2 (50 mL min^{-1}) at 700 °C for 2 h to obtain Mo–N/support. After cooling to ambient temperature, Ar gas flow was used to purge

the sample for 1 h. The purge was followed by the adsorption of H_2 step (under 5 vol% H_2 in Ar, 50 mL min^{-1}) and switched back to Ar (50 mL min^{-1}) for 1 h to remove all the physisorbed molecules of H_2. The H_2 desorption was conducted by increasing the temperature (1 °C/min) until reaching 700 °C under Ar flow (50 mL min^{-1}).

5.3. Catalytic Activity

5.3.1. Ammonia Synthesis

In a typical experiment, 0.2 g of 10-Mo–O/support was placed in a quartz reactor tube held centrally in a vertical furnace. Prior to the ammonia synthesis reaction, the sample was activated at 700 °C (10 °C min^{-1}) under 75 vol% H_2/N_2 (BOC, 99.98%) at 60 mL min^{-1} for 2 h to obtain the corresponding nitride X-Mo–N/support. After the activation step, the reactor was cooled down, and the reaction was performed at 400 °C and atmospheric pressure using the same gas mixture and gas flow.

The reactor effluent steam was flowed to a 200 mL of H_2SO_4 solution (0.0018 M), and ammonia production was calculated from the conductivity variation rate. The catalytic activity was monitored as a function of reaction time.

5.3.2. Ammonia Decomposition

The performance of 10-Mo–N/support catalysts in ammonia decomposition reaction was investigated under a 15 vol% NH_3/Ar (BOC, 99.98%) gas mixture at a total gas flow of 100 mL min^{-1}. The reaction was carried out in a quartz reactor containing 0.6 g of catalyst that was subject to a similar activation step as in the ammonia synthesis test. After activation 700 °C, the catalyst was cooled to ambient temperature under 75 vol% H_2/N_2. The catalytic activity was then measured between 250 and 700 °C by steps of 100 °C (30 min at each step) from 250 to 450 °C and then by steps of 50 °C (30 min at each step) from 450 to 700 °C. Ammonia conversion was determined using an FTIR analyzer.

Acknowledgements

The authors acknowledge the CNRS, the Chevreul Institute (FR 2638), the Ministère de l'Enseignement Supérieur et de la Recherche, the Région Hauts-de-France, the FEDER, and the MEL for supporting this work. The authors would like to thank the University of Lille for PhD granting (Amanda Sfeir) and I-Site ULNE for partially supporting this work. Said Laassiri would like to thank UM6P for support and funding, Pardis Simon for XPS data acquisition and chamber treatment, and Anne-Marie Blanchenet for TEM sample preparation.

Conflict of Interests

The authors declare no conflict of interest.

Data Availability Statement

The data that support the findings of this study are available from the corresponding author upon reasonable request.

Keywords: Ammonia decomposition · Ammonia synthesis · Molybdenum nitride · Nanoparticles · SMSI effect

[1] S. Giddey, S. P. S. Badwal, C. Munnings, M. Dolan, *ACS Sustain. Chem. Eng.* **2017**, *5*, 10231–10239.
[2] a) A. Boretti, S. Castelletto, *ACS Energy Lett.* **2022**, *7*, 2557–2564; b) B. Stolz, M. Held, G. Georges, K. Boulouchos, *Nat. Energy* **2022**, *7*, 203–212.
[3] G. Jeerh, M. Zhang, S. Tao, *J. Mater. Chem. A* **2021**, *9*, 727–752.
[4] a) C. Leterme, C. Fernández, P. Eloy, E. M. Gaigneaux, P. Ruiz, *Catal. Today* **2017**, *286*, 85–100; b) C. Fernández, N. Bion, E. M. Gaigneaux, D. Duprez, P. Ruiz, *J. Catal.* **2016**, *344*, 16–28; c) S. Dahl, A. Logadottir, R. C. Egeberg, J. H. Larsen, I. Chorkendorff, E. Törnqvist, J. K. Nørskov, *Phys. Rev. Lett.* **1999**, *83*, 1814–1817; d) K. Honkala, A. Hellman, I. N. Remediakis, A. Logadottir, A. Carlsson, S. Dahl, C. H. Christensen, J. K. Nørskov, *Science* **2005**, *307*, 555–558.
[5] a) K. Aika, A. Ohya, A. Ozaki, Y. Inoue, I. Yasumori, *J. Catal.* **1985**, *92*, 305–311; b) K.-i. Aika, *Angew. Chem. Int. Ed. Engl.* **1986**, *25*, 558–559.
[6] a) Z. Wang, J. Lin, R. Wang, K. Wei, *Catal. Commun.* **2013**, *32*, 11–14; b) B. Lin, Y. Liu, L. Heng, X. Wang, J. Ni, J. Lin, L. Jiang, *Ind. Eng. Chem. Res.* **2018**, *57*, 9127–9135; c) Y. Kobayashi, Y. Tang, T. Kageyama, H. Yamashita, N. Masuda, S. Hosokawa, H. Kageyama, *J. Am. Chem. Soc.* **2017**, *139*, 18240–18246; d) Y. Inoue, M. Kitano, S.-W. Kim, T. Yokoyama, M. Hara, H. Hosono, *ACS Catal.* **2014**, *4*, 674–680; e) Y. Lu, J. Li, T. Tada, Y. Toda, S. Ueda, T. Yokoyama, M. Kitano, H. Hosono, *J. Am. Chem. Soc.* **2016**, *138*, 3970–3973.
[7] a) A. N. Varakin, A. V. Mozhaev, A. A. Pimerzin, P. A. Nikulshin, *Appl. Catal. B* **2018**, *238*, 498–508; b) H. Topsøe, B. S. Clausen, *Appl. Catal.* **1986**, *25*, 273–293.
[8] a) M. M. H. Mondol, B. N. Bhadra, S. H. Jhung, *Appl. Catal. B* **2021**, *288*, 119988; b) J. Zou, Y. Lin, S. Wu, Y. Zhong, C. Yang, *Adv. Funct. Mater.* **2021**, *31*, 2100442.
[9] a) S. Singh, A. Modak, K. K. Pant, A. Sinhamahapatra, P. Biswas, *ACS Appl. Nano Mater.* **2021**, *4*, 8644–8667; b) Y. Kuwahara, T. Mihogi, K. Hamahara, K. Kusu, H. Kobayashi, H. Yamashita, *Chem. Sci.* **2021**, *12*, 9902–9915.
[10] a) R. Kojima, K.-i. Aika, *Appl. Catal. A* **2001**, *218*, 121–128; b) L. Volpe, M. Boudart, *J. Phys. Chem.* **1986**, *90*, 4874–4877; c) S. T. Oyama, *Catal. Today* **1992**, *15*, 179–200.
[11] W. Zheng, T. P. Cotter, P. Kaghazchi, T. Jacob, B. Frank, K. Schlichte, W. Zhang, D. S. Su, F. Schüth, R. Schlögl, *J. Am. Chem. Soc.* **2013**, *135*, 3458–3464.
[12] a) C. J. H. Jacobsen, *Chem. Commun.* **2000**, 1057–1058; b) I. AlShibane, A. Daisley, J. S. J. Hargreaves, A. L. Hector, S. Laassiri, J. L. Rico, R. I. Smith, *ACS Sustain. Chem. Eng.* **2017**, *5*, 9214–9222; c) S. Al Sobhi, N. Bion, J. S. J. Hargreaves, A. L. Hector, S. Laassiri, W. Levason, A. W. Lodge, A. R. McFarlane, C. Ritter, *Mater. Res. Bull.* **2019**, *118*, 110519; d) S. Al Sobhi, J. S. J. Hargreaves, A. L. Hector, S. Laassiri, *Dalton Trans.* **2019**, *48*, 16786–16792.
[13] a) R. Kojima, K. Aika, *Appl. Catal. A Gen.* **2001**, *219*, 141–147; b) N. Liu, L. Nie, N. Xue, H. Dong, L. Peng, X. Guo, W. Ding, *ChemCatChem* **2010**, *2*, 167–174; c) A. Sfeir, C. Abreu Teles, M. Marinova, H. Vezin, A. Lofberg, J.-p. Dacquin, S. Laassiri, S. Royer, *Faraday Discuss.* **2023**; 243, 126-147; d) B. Fang, C. Zhang, Z. Qi, C. Li, J. Ni, X. Wang, J. Lin, C.-T. Au, B. Lin, L. Jiang, *AIChE J.* **2022**, *68*, e17849.
[14] D. McKay, J. S. J. Hargreaves, J. L. Rico, J. L. Rivera, X. L. Sun, *J. Solid State Chem.* **2008**, *181*, 325–333.
[15] A. Ungureanu, B. Dragoi, A. Chirieac, C. Ciotonea, S. Royer, D. Duprez, A. S. Mamede, E. Dumitriu, *ACS Appl. Mater. Interfaces* **2013**, *5*, 3010–3025.
[16] J. Baltrusaitis, B. Mendoza-Sanchez, V. Fernandez, R. Veenstra, N. Dukstiene, A. Roberts, N. Fairley, *Appl. Surf. Sci.* **2015**, *326*, 151–161.
[17] L. Huo, X. Han, L. Zhang, B. Liu, R. Gao, B. Cao, W.-W. Wang, C.-J. Jia, K. Liu, J. Liu, J. Zhang, *Appl. Catal. B* **2021**, *294*, 120254.
[18] P. Burroughs, A. Hamnett, A. F. Orchard, G. Thornton, *J.Chem. Soc. Dalton Trans.* 1686–1698.

[19] T. Bhaskar, K. R. Reddy, C. P. Kumar, M. R. V. S. Murthy, K. V. R. Chary, *Appl. Catal. A* **2001**, *211*, 189–201.
[20] S. Watanabe, X. Ma, C. Song, *J. Phys. Chem. C* **2009**, *113*, 14249–14257.
[21] K. Sohlberg, S. T. Pantelides, S. J. Pennycook, *J. Am. Chem. Soc.* **2001**, *123*, 6609–6611.
[22] K.-i. Aika, A. Ozaki, *J. Catal.* **1969**, *14*, 311–321.
[23] N. Perret, D. Lamey, L. Kiwi-Minsker, F. Cárdenas-Lizana, M. A. Keane, *Catal. Sci. Technol.* **2019**, *9*, 1891–1901.
[24] a) F. Cárdenas-Lizana, D. Lamey, L. Kiwi-Minsker, M. A. Keane, *J. Mater. Sci.* **2018**, *53*, 6707–6718; b) A. Lilić, L. Cardenas, A. Mesbah, E. Bonjour, P. Jame, C. Michel, S. Loridant, N. Perret, *J. Alloys Compd.* **2022**, *924*, 166576.
[25] F. Cárdenas-Lizana, S. Gómez-Quero, N. Perret, L. Kiwi-Minsker, M. A. Keane, *Catal. Sci. Technol.* **2011**, *1*, 794–801.
[26] a) J.-G. Choi, R. L. Curl, L. T. Thompson, *J. Catal.* **1994**, *146*, 218–227; b) S. Jujjuri, F. Cárdenas-Lizana, M. A. Keane, *J. Mater. Sci.* **2014**, *49*, 5406–5417.
[27] V. T. T. Ha, A. Sarıoğlan, A. Erdem-Şenatalar, Y. B. Taârit, *J. Mol. Catal. A Chem.* **2013**, *378*, 279–284.
[28] J. J. Birtill, P. G. Dickens, *J. Solid State Chem.* **1979**, *29*, 367–372.
[29] D. Zhao, J. Sun, Q. Li, G. D. Stucky, *Chem. Mater.* **2000**, *12*, 275–279.

Manuscript received: March 12, 2024
Revised manuscript received: September 25, 2024
Accepted manuscript online: October 28, 2024
Version of record online: ■■, ■■